Energy &
Environmental
Science

rsc.li/ees

Volume 11
Number 4
April 2018
Pages 719-1000

ISSN 1754-5706

REVIEW ARTICLE
Yuekun Lai, Zhiqun Lin et al.
Graphene aerogels for efficient energy storage and conversion

ROYAL SOCIETY
OF CHEMISTRY

ROYAL SOCIETY
OF CHEMISTRY

rsc.li/ees

COMMUNICATION

Ultrafast laser-annealing of perovskite films for efficient perovskite solar cells

Peng You, Guijun Li, Guanqi Tang, Jiupeng Cao and Feng Yan*

Perovskite solar cells have attracted much attention recently for their high efficiency, ease of preparation and low cost. Here, we report a novel laser-annealing method for perovskite films at a low substrate temperature by scanning laser spots on the film surfaces. An ultrafast crystallization process within a few seconds is realized under a laser with a high intensity and a fast scanning speed. Because the crystalline perovskite phase has a stronger light absorption than the amorphous phase, the fast laser annealing can induce a higher temperature in the former and lead to the selective growth of large perovskite grains. Under optimum conditions, perovskite films with high crystallinity are successfully fabricated, resulting in perovskite solar cells with high power conversion efficiency and good stability. Moreover, a faster laser-annealing process of perovskite films is achieved by using a linear laser beam, which is expected to be a promising technique for the mass production of large-scale perovskite solar cells.

Introduction

Organic-inorganic hybrid perovskite solar cells (PSCs) have attracted tremendous attention in recent years due to their high power conversion efficiency (PCE) and low fabrication cost. The unique properties of the organic-inorganic hybrid perovskites, like the high light absorption coefficient[1-6], high carrier mobilities[7-9], small exciton binding energy[10-12] and long carrier diffusion lengths[13-16], are responsible for the high photovoltaic performance of PSCs. Since the first report of PSCs with a PCE of 3.8% in 2009, the certified efficiency was improved rapidly to over 25% in the past decade.[17-28] The crystallinity of perovskite films has been found to be critical to the device performance.[29-36] Perovskite films with larger grains normally have lower density of trap states and higher carrier mobilities, which can lead to reduced carrier recombination and enhanced photovoltaic performance of PSCs. [29-35] The annealing

conditions of perovskite films are detrimental to the growth of perovskite grains.[29, 33, 37-39] However, it is challenging to precisely control the crystallization of perovskite films based on a conventional thermal annealing method. Besides, a thermal-annealing process is time and energy consuming, and it is incompatible with low-temperature fabrication required by certain devices such as flexible PSCs on plastic substrates. Therefore, the perovskite annealing process can be a bottleneck for the mass-production of PSCs, and novel annealing approaches are desirable to overcome these limitations.

Laser-annealing techniques have been successfully used in semiconductor industry for the mass production of large-scale devices. They can be utilized for the treatment of various materials, like silicon, metal oxides and nanomaterials,[40-47] and demonstrate numerous advantages over thermal annealing, including controllable crystallization, low-temperature processing, large-area fabrication and being a non-contact process.[40, 41, 48] More importantly, an ultrafast annealing process can be achieved on large-area samples by scanning the laser beams on their surfaces, which can hardly be realized with other heating methods. Complex patterns can be produced by scanning the laser spot in a programmable path with computer-aided designs. Furthermore, a suitable temperature gradient induced by localized laser-annealing can be favorable for crystal growth.[16, 49, 50] Although some attempts of using laser to anneal perovskite films have been reported, no high-performance PSCs have been realized based on the technology until now.[51, 52] Besides, photonic flash annealing of perovskite films has been demonstrated by using white light[53] or infrared light[54]. However, these methods will induce high substrate temperatures, and the device efficiencies are even lower than those of the control devices.

In this work, we developed a novel annealing approach for methylammonium lead iodide ($MAPbI_3$) and $(CsPbI_3)_{0.05}(FAPbI_3)_{0.95}(MAPbBr_3)_{0.05}$ mixed perovskite films by fast laser beam scanning. The laser-annealing process was optimized by tuning the laser scanning conditions, including laser wavelength, scanning speed and output power. The laser-annealed perovskite films demonstrate larger grain sizes than thermal-annealed samples,

Department of Applied Physics, The Hong Kong Polytechnic University, Hung Hom, Kowloon, Hong Kong.
E-mail: apafyan@polyu.edu.hk

which can be attributed to the temperature gradient generated between perovskite seeds and the amorphous components around them due to different light absorption coefficients of the two phases. Under optimum conditions, the average PCE of the devices is relatively improved for about 20% in comparison with the control devices prepared by thermal annealing. By using a linear laser beam, large-area devices can be prepared with a high speed, which paves a way for the mass production of PSCs at a low temperature.

Results and discussion

Figure 1a shows the schematic illustration of the laser annealing process. MAPbI$_3$ perovskite films were prepared by using a typical antisolvent-assisted spin-coating method. Then, a robotic laser scanning system (See supporting information, **Figure S1a**) was used to anneal the as-deposited perovskite films. A continuous-wave diode laser with controllable output power was fixed on an X-Y motorized stage. The downward laser beam can scan along a designed track on the sample surface with a speed (See supporting information, **Figure S1b**) under the control of a computer program. The laser spot on film surface was controlled to have a diameter of 1.0 mm. Laser diodes with different wavelengths (405 nm, 450 nm and 660 nm) were used in film annealing. Notably, as-deposited perovskite films were light brown, indicating that they were partially crystalized before annealing. The coexistence of crystalline and amorphous phases in as-deposited perovskite films was also confirmed by X-ray diffraction (XRD) patterns (See supporting information, **Figure S2**). After the laser scanning processes, perovskite films were completely crystallized and turned into black, as shown in **Figure 1a**.

The surface temperature distribution of a perovskite film was monitored by an infrared thermal imager (inset in **Figure 1b**) during the laser annealing process (wavelength: 450 nm). **Figure 1b** and **1c** show the 2-dimentional (2D) and 3-dimentional (3D) infrared thermal images of the perovskite film surface. The laser output power and the scanning speed here are 150 mW and 25 mm/min, respectively. It is noteworthy that only a small local area near the laser beam center shows an apparent higher temperature than the other part of the surface. **Figure 1d** shows the temperature distribution along the dash line passing through the laser beam center in **Figure 1c**. The maximum temperature of the perovskite surface is 100 ºC, which is equal to the optimum thermal annealing temperature of a MAPbI$_3$ perovskite film on a hotplate (See supporting information, **Figure S3**).[29, 55-57] For other laser beams with different wavelengths (405 nm and 660 nm), the central temperatures on perovskite surfaces can also be controlled at the same value by tuning the output power (See supporting information, **Figure S4**). Notably, the substrate temperature we measured on the back surface is equal to the room temperature because the laser is only absorbed on the top surface of the perovskite film. So the substrate temperature is not increased by the laser annealing, which is critical to some substrates that cannot sustain high temperatures.

Figure 1e presents the XRD spectra of the thermal-annealed and laser-annealed films (laser wavelength: 450 nm). All diffraction peaks (apart from those peaks from the fluorine doped tin oxide (FTO)/TiO$_2$ substrate) belong to the MAPbI$_3$ tetragonal phase, indicating that both films were well crystalized after the annealing processes. We can find that the (110) main diffraction peak shows a higher peak intensity than the other peaks corresponding to other lattice planes. The peak intensity ratios of (110) peaks over some other diffraction peaks of the laser-annealed film are much higher than those of the thermal-annealed film (see supporting information, **Table S1**), indicating that a preferred orientation along (110) direction has been obtained in the former. Notably, the highly oriented perovskite films prepared by laser annealing are favorable for exciton dissociation, charge transfer and diffusion.[24, 58, 59]

In addition to the annealing of as-deposited perovskite films, the laser scanning system can be used for precisely patterning crystalline perovskite films. As shown in **Figure 1f**, the well crystallized perovskite film can be patterned with the laser beam based on a design from the control system (the inset picture). When the laser beam is focused on the sample surface to a tiny point, the localized high temperature can decompose the crystalline perovskite film following a reaction of $CH_3NH_3PbI_3 \rightarrow PbI_2 + CH_3NH_3I$ (vapor).[60] So a layer of PbI$_2$ can be obtained after the laser-patterning, as confirmed by the XRD pattern (see supporting information, **Figure S5**). The laser-patterning technique may find applications for large-scale module processing of PSCs or light emitting diodes (LEDs) based on perovskite films.

Figure 2 shows the plan-view SEM images of the perovskite films fabricated by thermal-annealing and laser-annealing. The statistical diagrams of the grain size distribution based on the SEM images are presented in the insets. Laser beams of different wavelengths (405 nm, 450 nm and 660 nm) were driven at the same scanning speed (25 mm/min) with the same central temperature (100 °C) on perovskite films. It is obvious that the average grain sizes of the laser-annealed perovskite films are much larger than that of the thermal-annealed film. The cross-sectional SEM images of the perovskite films shown in **Figure S6** also demonstrate that most of the perovskite grains were penetrating through the perovskite capping layer, and most of the grain boundaries were perpendicular to the substrate, which is beneficial for charge transport from perovskite to charge collection layers. Moreover, this microstructure may result in a reduced surface area of the grain boundaries and a low concentration of defects in the perovskite films. So nonradiative charge carrier recombination in the perovskite films can be alleviated, which will lead to enhanced photovoltaic performance of the PSCs.[35, 58, 61]

To better understand the laser-annealing effect, UV-visible absorption spectra of the as-deposited and laser-annealed perovskite films were characterized, as presented in **Figure 2e**. The light absorption of the perovskite film is much higher than that of the as-deposited film at any wavelength, indicating that the perovskite grains or seeds can absorb more energy from the laser and have

higher temperatures than the surrounding amorphous phase, as illustrated in **Figure 2f**. The laser spot was scanned on the surface with a high speed (25 mm/min), the actual annealing time for each point is estimated to be 1.5 s (See supporting information, **Figure S7**). Notably, the surface temperature can be increased to 100 °C in a few seconds with the rate up to 43 °C/s. During the fast laser annealing process, localized temperature gradient on the boundaries of perovskite grains can be generated, which acts as a driving force for the growth of perovskite grains. Large grains can absorb more energy and have higher temperatures than small grains, which can induce the selective growth of the large grains. However, for thermal-annealing, heat is transferred from the bottom glass/FTO/TiO$_2$ substrate to the upper perovskite film, and it can be uniformly absorbed by both the crystalline and the amorphous phases of the perovskite film, leading to a high density of nucleation seeds in the films upon annealing. Therefore, the fast laser-annealing approach can result in larger grains than the thermal annealing process.

Notably, the crystallinity of the laser-annealed perovskite films is closely related to the laser wavelength. The average grain sizes were different when three different lasers (wavelength: 405 nm, 450 nm and 660 nm) were used in the annealing processes and 450-nm laser led to the largest average grain size of ~ 476 nm (See supporting information, **Table S2**). We consider that this effect can be attributed to the different light absorption coefficients of the perovskite films at different wavelengths. It is noteworthy that the absorbance ratio of the two absorption spectra shown in Figure 2e changes with the light wavelength and peaks at around 450 nm. Therefore, the 450-nm laser can induce the biggest temperature gradient on grain boundaries in perovskite films and provide the largest growth driving force for the perovskite seeds in the as-deposited film.

We have studied the influence of scanning speed and laser output power on the morphology of the perovskite films. For the fixed power (150 mW) of the laser, the grain size increased with the decrease of scanning speed and then decreased when the speed was less than 25 mm/min (see supporting information, **Figure S8**). We found that the surface temperature increased with the decrease of scanning speed and the largest grain size was obtained when the central temperature was 100 °C (see supporting information, **Figure S9**). For a fixed scanning speed of 25 mm/min, the crystallinity increased with the increase of output power and then decreased when the power was over 150 mW (see supporting information, **Figure S10**). The corresponding surface temperature as a function of output power was also obtained (see supporting information, **Figure S11**). Both experiments indicated that the maximum grain size was achieved at the central temperature of 100 °C, which is consistent with the condition required by a thermal annealing process.

We then prepared PSCs with a device configuration of glass/FTO/compact TiO$_2$ (c-TiO$_2$)/mesoporous TiO$_2$ (mp-TiO$_2$)/perovskite/spiro-OMeTAD/Au, as shown in **Figure 3a**. Current density-voltage (*J-V*) curves of the devices prepared by laser-annealing and thermal-annealing (control) processes are presented

in **Figure 3b**. The detailed photovoltaic parameters of the PSCs are summarized in **Table 1**. All parameters are considerably improved for the PSCs fabricated by laser-annealing processes in comparison with the control devices processed by thermal annealing. The control devices show an average PCE of 16.89%, V_{oc} of 1.069 V, short circuit current density (J_{sc}) of 22.36 mA/cm^2 and fill factor (FF) of 70.64%. In contrast, the 405-nm laser treated devices show an enhanced average PCE of 19.71%, V_{oc} of 1.112 V, J_{sc} of 23.18 mA/cm^2 and FF of 76.44%. The average efficiency is further increased to 19.92% with V_{oc} of 1.119 V, J_{sc} of 23.22 mA/cm^2, and FF of 76.68% by using 660-nm laser. The device performance is maximized when 450-nm laser is adopted, demonstrating an average PCE of 20.23%, V_{oc} of 1.124 V, J_{sc} of 23.29 mA/cm^2 and FF of 77.27%. The greatly enhanced device performance by laser annealing is consistent with the improved crystallinity of the laser-annealed perovskite films. Notably, the champion device by laser-annealing shows PCE of 20.98% (19.90%), V_{oc} of 1.13 V (1.125 V), J_{sc} of 23.41 mA/cm^2 (23.41 mA/cm^2) and FF of 79.3% (75.5%) for reverse (forward) scan. **Figure 3c** presents the corresponding EQE spectra, demonstrating an improved quantum efficiency in the whole wavelength range for the champion device. The integrated photocurrent from the EQE spectra is in good agreement with the J_{sc} derived from the *J-V* curves in **Figure 3b**.

For the champion device, a steady-state efficiency of 20.20% was achieved at the maximum power point of 0.96 V (See supporting information, **Figure S12**). Besides, we also collected the statistical data of devices (40 devices for each condition) prepared by using the optimized laser-annealing and thermal-annealing approaches, respectively, as shown in **Figure 3d**. The target devices have an average efficiency of 20.23%, which is much higher than that of the control devices (16.89%). It is notable that the PCEs of the target devices are distributed in a narrow range from 19.41% to 20.98%, showing good reproducibility.

We further investigated the influences of the laser scanning speeds and laser output power on the device performance (laser wavelength: 450 nm) (See supporting information, **Figure S13** and **Table S3-S4)**. The effects of laser scanning speed and laser power on the device performance were quite similar. With the increase of the laser scanning speeds from 10 mm/min to 100 mm/min (or the laser output power from 110 mW to 170 mW), the average PCEs were firstly increased and subsequently decreased with a maximum value of 20.23% at the scanning speed of 25 mm/min and the laser power of 150 mW, which is consistent with the condition for obtaining the biggest perovskite grain size. These results suggest that the photovoltaic performance of the PSCs is closely related to the crystallinity of the laser-annealed perovskite films.

To gain a deeper insight into the nature of the outstanding photovoltaic performance of the PSCs prepared by laser-annealing approach, we performed steady-state and time-resolved photoluminescence (PL) measurements of the perovskite films prepared at different conditions, as shown in **Figure 4a** and **4b**. The perovskite films for PL measurements were fabricated on pure glass

substrates without FTO layers. It is notable that the optimized laser-annealed perovskite film exhibited more than three-fold increase in PL intensity relative to that of the thermal-annealed film. Meanwhile, the PL peak demonstrated a slight blue shift from 768 nm (thermal-annealing) to 766 nm (laser-annealing). The enhanced PL intensity and the blue-shifted PL peak stem from the decreased bulk defect density in the perovskite absorber, which can lead to reduced charge recombination.[24, 57, 62] To analyze the dynamics of the charge recombination in the perovskite films, time-resolved PL decay measurements were also performed. The PL decay processes for thermal-annealed and laser-annealed perovskite films were shown in **Figure 4b**. A much slower PL decay can be found in the laser-annealed film. The decay curves were fitted with a biexponential function: $Y = A_1 \exp(-t/\tau_1) + A_2 \exp(-t/\tau_2)$.[24] The fast decay lifetime (τ_1) was attributed to the nonradiative recombination in the region with high-density defects such as the film surface, while the slow decay lifetime (τ_2) was ascribed to the recombination in the region with lower density of defects.[24, 49] The laser-annealed perovskite film displayed the two decay lifetimes of $\tau_1 = 51.9\ ns$ and $\tau_2 = 193.6\ ns$. In contrast, the thermal-annealed film exhibited much shorter lifetimes: $\tau_1 = 17.3\ ns$ and $\tau_2 = 45.6\ ns$. The longer PL lifetimes of the laser-annealed perovskite films imply the decreased concentrations of defects and traps, which can result in an increased short-circuit current and a higher open-circuit voltage of a PSC.[24, 35, 58]

Electrochemical impedance spectroscopy (EIS) measurements of the PSCs were performed under light illumination of 100 mW/cm². **Figure 4c** shows the EIS spectra of the devices at a bias voltage of 0.8 V. A big half circle corresponding to charge recombination process can be found in the Nyquist plot. The target device exhibits a much larger recombination resistance (~ 639.6 Ω) than that of the control device (~ 271.3 Ω), indicating reduced charge recombination in the perovskite films or at the interfaces between perovskite and charge transport layers.[63-65] **Figure 4d** shows the recombination resistance (R_{rec}) values at different applied voltages under light illumination of 100 mW/cm² (derived from the impedance spectra in **Figure S14**). It is notable that R_{rec} was larger for the target device at any bias voltage than that for the control device, indicating a slower recombination rate in the target device, which can be attributed to the lower density of trap states in the laser-annealed perovskite film. Furthermore, the increased R_{rec} will contribute to the shunt resistance of the solar cells, which is a main reason for the increased FF of the target devices.

We also investigated the long-term stability of the PSCs fabricated by laser-annealing and thermal-annealing processes. The encapsulated devices were kept in air with a relative humidity ~ 30% for stability study. *J-V* curves of the devices were characterized for every 240 h. The statistical data of the PCEs after degradation for 1200 h was shown in **Figure S15**. Apparently, the devices fabricated by laser-annealing were much more stable than the control devices. The target devices maintained about 90% of its initial average PCE after the storage for 1200 h, while the control devices retained only 78% of the original efficiency. The improved stability of the target devices

can be attributed to the improved crystallinity of the laser-annealed perovskite films.

To realize faster laser annealing of perovskite films, we then used linear laser beams in our experiments, which was generated by introducing a cylindrical convex lens. **Figure S16a** shows the schematic diagram of the laser annealing process of the as-deposited perovskite films by using a linear laser beam. **Figure S16b** shows the infrared thermal image of the as-deposited perovskite film surface during linear laser scanning (wavelength: 450 nm, step distance: 2 mm). The temperature distribution close to the linear laser beam along two vertical directions is shown in **Figure S17**. The high temperature region (> 70 °C) is about 5 mm. So it is much faster to anneal a sample by using the linear laser than a laser spot. The *J-V* curve of the champion small-area PSC prepared by the linear laser annealing is shown in **Figure S16c**. The device shows a high efficiency of 20.25%, V_{oc} of 1.115 V, J_{sc} of 23.04 mA/cm², and FF of 78.8% (derived from the reverse scan curve). By using this linear laser scanning process, we also prepared large-area PSCs with an active area of 1.0 cm². The device photo and corresponding *J-V* curves of the laser-annealed PSCs are shown in **Figure S16d**. The laser-annealed PSC exhibits a relatively high efficiency of 17.26%, which is 13.7% higher than that of the thermal-annealed device (15.18%), as shown in **Table S5**. So we can compare the laser-annealing time with the thermal-annealing time reported in the literature.[19-22, 24, 29-32, 34-37] For a device with the size of 1cm × 1cm, the laser-annealing time is estimated to be ~ 24 s, which is much shorter than the conventional thermal-annealing time on a hotplate (tens of minutes). Importantly, this technique can be scaled up for a much higher throughput simply by using more or bigger laser sources. In addition, the power consumption for laser-annealing can be far less than that of thermal-annealing. Therefore, the cheap and fast laser-annealing technique is promising for the large-scale fabrication of high-efficiency PSCs.

In addition to the MAPbI₃-based PSCs, (CsPbI₃)₀.₀₅(FAPbI₃)₀.₉₅(MAPbBr₃)₀.₀₅ mixed PSCs were also prepared by using laser-annealing approach. The as-deposited mixed perovskite films were annealed by scanning laser beams with wavelengths of 405 nm, 450 nm or 660 nm. The surface temperature distribution of the mixed perovskite film was monitored by the infrared thermal imager (See supporting information, **Figure S18**). We then prepared mixed PSCs with the same device structure as the above mentioned MAPbI₃-based PSCs. The device performance was then optimized by controlling the laser power. Under the optimum conditions, we found that the maximum surface temperatures of the perovskite films are all close to 150 °C (equal to the optimum thermal-annealing temperature of the control device). Similarly, only a very small area of the perovskite film surface near the beam center shows relatively high temperature, while the surface temperature of the other part of the film is close to the room temperature. The maximum heating rate is about 100 °C/s, which cannot be achieved by a normal thermal annealing method. (See supporting information, **Figure S19**).

Figure 5 shows the SEM images of the mixed perovskite films prepared by thermal-annealing (150 ºC for 10 min) and laser-annealing processes. The average grain sizes of the laser-annealed perovskite films (1.84 μm for 450-nm laser, 1.5 μm for 660-nm laser, and 1.38 μm for 405-nm laser) are much larger than that of the control film prepared by thermal-annealing (0.88 μm) (See supporting information, Table S6), which is consistent with the result of MAPbI$_3$ perovskite films. More importantly, the grain size is closely related with the laser wavelength. Therefore, we checked the UV-visible absorbance spectra of the as-deposited and laser-annealed mixed perovskite films (See supporting information, **Figure S20**). Notably, the absorbance ratio between the two films varies with the light wavelength and peaks at around 450 nm. At this condition, the average grain size is the maximum, which further confirms that the temperature gradient in the film is critical to the growth of perovskite grains. As explained above, the 450-nm laser can provide the largest growth driving force for the perovskite seeds in the as-deposited films. As a result, perovskite films annealed with 450-nm laser show largest average grain size.

Figure 5e shows the *J-V* curves of the devices fabricated by thermal-annealing and laser-annealing processes. Detailed photovoltaic parameters are summarized in **Table 2**. Notably, the device performance is better for the devices with larger perovskite grains. A high V_{oc} of 1.175 V and high PCE of 21.5% were achieved when 450-nm laser was used for the laser-annealing process. The champion device can get a steady-state efficiency of 21.2%, as shown in **Figure 5f**. Moreover, the optimized devices also show negligible hysteresis and increased quantum efficiency (See supporting information **Figure S21** and **Table S7**).

The quality of the perovskite films can be reflected by the Urbach energy (E_u), which is normally related to the impurities, ionic disorder and atomic vibrational fluctuations in the films.[66-70] We have calculated the Urbach energy according to the EQE spectra of the best MAPbI$_3$ and mixed PSCs (See supporting information **Figure S22**). Based on the equation of EQE = EQE$_0$ exp [($E - E_g$)/E_u] (where EQE$_0$ is the EQE value at the bandgap), the slope of the exponential EQE tail defines the Urbach energy.[67, 68] The derived Urbach energy values are shown in **Table S8**. Notably, both MAPbI$_3$ and mixed PSCs prepared by laser-annealing technique show slightly lower Urbach energies (18.3 meV and 14.2 meV) than those obtained from thermal-annealing method (19.8 meV and 15.7 meV), indicating better quality of the laser-annealed perovskite films, which leads to the increased V_{oc} of the PSCs prepared by laser-annealing processes.[66-70]

Besides, we tested the device stability of the mixed PSCs under both dark or light illumination conditions (See supporting information **Figure S23**). After storing in dark for about 2000 hours, there was no obvious decrease in PCE for the device prepared by laser-annealing process, while the PCE of the control device can only retain 85% of the original value. Even under light illumination of 100 mW/cm^2 (AM 1.5G), the devices prepared by laser-annealing can maintain 95% of the initial PCE after light soaking test for over 200 hours, while the control devices lost about half of its value. The greatly improved device stability of the PSCs prepared by laser-annealing should be ascribed to the increased crystallinity of the perovskite films.

Conclusions

In summary, we have developed an ultrafast laser annealing approach for the preparation of both MAPbI$_3$ and mixed perovskite films at room temperature. Perovskite films were crystalized under high-intensity laser in a few seconds and the average grain size was controlled by tuning the laser wavelength, scanning speed and output power. Under optimum conditions, high-quality perovskite films with good crystallinity, preferred orientation and low density of defects were successfully fabricated. We consider that the different light absorption coefficients in perovskite grains and amorphous phases can induce temperature gradient at the boundaries of perovskite grains under the laser annealing. The temperature gradient can act as a driving force for the crystallization of perovskite grains and lead to larger grain sizes than the conventional thermal annealing method. Furthermore, a linear laser beam has been successfully used to achieve a fast annealing process in a large area, which would be highly compatible with the mass production of PSCs.

Conflicts of interest

There are no conflicts to declare.

Acknowledgements

References

1. S. Yakunin, M. Sytnyk, D. Kriegner, S. Shrestha, M. Richter, G. J. Matt, H. Azimi, C. J. Brabec, J. Stangl, M. V. Kovalenko and W. Heiss, *Nat. Photonics*, 2015, **9**, 444.
2. W. J. Yin, T. T. Shi and Y. F. Yan, *Adv. Mater.*, 2014, **26**, 4653.
3. H. S. Jung and N. G. Park, *Small*, 2015, **11**, 10-25.
4. C. Xie, P. You, Z. K. Liu, L. Li and F. Yan, *Light Sci. Appl.*, 2017, **6**, 17023.
5. D. C. Yang, C. Xie, J. H. Sun, H. Zhu, X. H. Xu, P. You, S. P. Lau, F. Yan and S. F. Yu, *Adv. Opt. Mater.*, 2016, **4**, 1053.
6. D. C. Yang, C. Xie, X. H. Xu, P. You, F. Yan and S. F. Yu, *Adv. Opt. Mater.*, 2018, **6**, 1700992.
7. T. Leijtens, S. D. Stranks, G. E. Eperon, R. Lindblad, E. M. J. Johansson, I. J. McPherson, H. Rensmo, J. M. Ball, M. M. Lee and H. J. Snaith, *ACS Nano*, 2014, **8**, 7147.
8. C. Wehrenfennig, G. E. Eperon, M. B. Johnston, H. J. Snaith and L. M. Herz, *Adv. Mater.*, 2014, **26**, 1584.
9. D. A. Valverde-Chavez, C. S. Ponseca, C. C. Stoumpos, A. Yartsev, M. G. Kanatzidis, V. Sundstrom and D. G. Cooke, *Energy Environ. Sci.*, 2015, **8**, 3700

COMMUNICATION

10. A. Miyata, A. Mitioglu, P. Plochocka, O. Portugall, J. T.-W. Wang, S. D. Stranks, H. J. Snaith and R. J. Nicholas, *Nat. Physics*, 2015, **11**, 582.

11. V. D'Innocenzo, G. Grancini, M. J. P. Alcocer, A. R. S. Kandada, S. D. Stranks, M. M. Lee, G. Lanzani, H. J. Snaith and A. Petrozza, *Nat. Commun.*, 2014, **5**, 3586.

12. K. Galkowski, A. Mitioglu, A. Miyata, P. Plochocka, O. Portugall, G. E. Eperon, J. T. W. Wang, T. Stergiopoulos, S. D. Stranks, H. J. Snaith and R. J. Nicholas, *Energy Environ. Sci.*, 2016, **9**, 962.

13. D. Shi, V. Adinolfi, R. Comin, M. J. Yuan, E. Alarousu, A. Buin, Y. Chen, S. Hoogland, A. Rothenberger, K. Katsiev, Y. Losovyj, X. Zhang, P. A. Dowben, O. F. Mohammed, E. H. Sargent and O. M. Bakr, *Science*, 2015, **347**, 519.

14. S. D. Stranks, G. E. Eperon, G. Grancini, C. Menelaou, M. J. P. Alcocer, T. Leijtens, L. M. Herz, A. Petrozza and H. J. Snaith, *Science*, 2013, **342**, 341.

15. G. C. Xing, N. Mathews, S. Y. Sun, S. S. Lim, Y. M. Lam, M. Gratzel, S. Mhaisalkar and T. C. Sum, *Science*, 2013, **342**, 344.

16. Q. F. Dong, Y. J. Fang, Y. C. Shao, P. Mulligan, J. Qiu, L. Cao and J. S. Huang, *Science*, 2015, **347**, 967.

17. A. Kojima, K. Teshima], Y. Shirai and T. Miyasaka, *J. Am. Chem. Soc.*, 2009, **131**, 6050.

18. H.-S. Kim, C.-R. Lee, J.-H. Im, K.-B. Lee, T. Moehl, A. Marchioro, S.-J. Moon, R. Humphry-Baker, J.-H. Yum, J. E. Moser, M. Grätzel and N. G. Park, *Sci. Rep.*, 2012, **2**, 591.

19. J. Burschka, N. Pellet, S. J. Moon, R. Humphry-Baker, P. Gao, M. K. Nazeeruddin and M. Gratzel, *Nature*, 2013, **499**, 316.

20. M. Liu, M. B. Johnston and H. J. Snaith, *Nature*, 2013, **501**, 395.

21. W. S. Yang, J. H. Noh, N. J. Jeon, Y. C. Kim, S. Ryu, J. Seo and S. I. Seok, *Science*, 2015, **348**, 1234.

22. M. Saliba, T. Matsui, J.-Y. Seo, K. Domanski, J.-P. Correa-Baena, M. K. Nazeeruddin, S. M. Zakeeruddin, W. Tress, A. Abate, A. Hagfeldt and M. Grätzel, *Energy Environ. Sci.*, 2016, **9**, 1989.

23. National Renewable Energy Laboratory (NREL), Best Research-Cell Efficiencies, https://www.nrel.gov/pv/cell-efficiency.html, (accessed October, 2019).

24. W. S. Yang, B. W. Park, E. H. Jung, N. J. Jeon, Y. C. Kim, D. U. Lee, S. S. Shin, J. Seo, E. K. Kim, J. H. Noh and S. I. Seok, *Science*, 2017, **356**, 1376.

25. P. You, G. Tang and F. Yan, *Materials Today Energy*, 2019, **11**, 128.

26. Q. D. Tai, X. Y. Guo, G. Q. Tang, P. You, T. W. Ng, D. Shen, J. P. Cao, C. K. Liu, N. X. Wang, Y. Zhu, C. S. Lee and F. Yan, *Angew Chem Int Edit*, 2019, **58**, 806.

27. Z. K. Liu, P. You, C. Xie, G. Q. Tang and F. Yan, *Nano Energy*, 2016, **28**, 151.

28. P. You and F. Yan, in *Ferroelectric Materials for Energy Applications*, ed. J. F. S. Haitao Huang, Wiley-VCH, Germany, 1 edition edn., 2019, p. 384.

29. Z. G. Xiao, Q. F. Dong, C. Bi, Y. C. Shao, Y. B. Yuan and J. S. Huang, *Adv. Mater.*, 2014, **26**, 6503.

30. W. J. Ke, C. X. Xiao, C. L. Wang, B. Saparov, H. S. Duan, D. W. Zhao, Z. W. Xiao, P. Schulz, S. P. Harvey, W. Q. Liao, W. W. Meng, Y. Yu, A. J. Cimaroli, C. S. Jiang, K. Zhu, M. Al-Jassim, G. J. Fang, D. B. Mitzi and Y. F. Yan, *Adv. Mater.*, 2016, **28**, 5214.

31. W. Zhang, S. Pathak, N. Sakai, T. Stergiopoulos, P. K. Nayak, N. K. Noel, A. A. Haghighirad, V. M. Burlakov, D. W. deQuilettes, A. Sadhanala, W. Z. Li, L. D. Wang, D. S. Ginger, R. H. Friend and H. J. Snaith, *Nat. Commun.*, 2015, **6**, 10030.

32. C. G. Wu, C. H. Chiang, Z. L. Tseng, M. K. Nazeeruddin, A. Hagfeldt and M. Gratzel, *Energy Environ. Sci.*, 2015, **8**, 2725.

33. W. Y. Nie, H. H. Tsai, R. Asadpour, J. C. Blancon, A. J. Neukirch, G. Gupta, J. J. Crochet, M. Chhowalla, S. Tretiak, M. A. Alam, H. L. Wang and A. D. Mohite, *Science*, 2015, **347**, 522.

34. C. Bi, Q. Wang, Y. C. Shao, Y. B. Yuan, Z. G. Xiao and J. S. Huang, *Nat. Commun.*, 2015, **6**, 7747.

35. X. Li, D. Q. Bi, C. Y. Yi, J. D. Decoppet, J. S. Luo, S. M. Zakeeruddin, A. Hagfeldt and M. Gratzel, *Science*, 2016, **353**, 58.

36. G. Tang, P. You, Q. Tai, A. Yang, J. Cao, F. Zheng, Z. Zhou, J. Zhao, P. K. L. Chan and F. Yan, *Adv. Mater.*, 2019, **31**, 1807689.

37. Y. W. Li, L. Meng, Y. Yang, G. Y. Xu, Z. R. Hong, Q. Chen, J. B. You, G. Li, Y. Yang and Y. F. Li, *Nat. Commun.*, 2016, **7**, 10214.

38. A. Dualeh, N. Tetreault, T. Moehl, P. Gao, M. K. Nazeeruddin and M. Gratzel, *Adv. Funct. Mater.*, 2014, **24**, 3250.

39. K. C. Tang, P. You and F. Yan, *Sol Rrl*, 2018, **2**, 1800075.

40. J. Lawrence, *Advances in laser materials processing: technology, research and applications*, Woodhead Publishing, Second edition. edn., 2018.

41. H. Palneedi, J. H. Park, D. Maurya, M. Peddigari, G. T. Hwang, V. Annapureddy, J. W. Kim, J. J. Choi, B. D. Hahn, S. Priya, K. J. Lee and J. Ryu, *Adv. Mater.*, 2018, **30**, 1705148.

42. J. S. Im, H. J. Kim and M. O. Thompson, *Appl. Phys. Lett.*, 1993, **63**, 1969.

43. M. A. Crowder, M. Moriguchi, Y. Mitani and A. T. Voutsas, *Thin Solid Films*, 2003, **427**, 101.

44. J. L. Ye, H. B. Tan, S. L. Wu, K. Ni, F. Pan, J. Liu, Z. C. Tao, Y. Qu, H. X. Ji, P. Simon and Y. W. Zhu, *Adv. Mater.*, 2018, **30**, 1801384.

45. G. Gonzalez-Rubio, P. Diaz-Nunez, A. Rivera, A. Prada, G. Tardajos, J. Gonzalez-Izquierdo, L. Banares, P. Llombart, L. G. Macdowell, M. A. Palafox, L. M. Liz-Marzan, O. Pena-Rodriguez and A. Guerrero-Martinez, *Science*, 2017, **358**, 640.

46. R. Q. Ye, Y. Chyan, J. B. Zhang, Y. L. Li, X. Han, C. Kittrell and J. M. Tour, *Adv. Mater.*, 2017, **29**, 1702211.

47. G. Qiu, Q. Nian, M. Motlag, S. Y. Jin, B. W. Deng, Y. X. Deng, A. R. Charnas, P. D. D. Ye and G. J. Cheng, *Adv. Mater.*, 2018, **30**, 1704405.

48. W. Staudt, S. Borneis and K. D. Pippert, *Phys. Status Solidi A*, 1998, **166**, 743.

49. Q. F. Han, S. H. Bae, P. Y. Sun, Y. T. Hsieh, Y. Yang, Y. S. Rim, H. X. Zhao, Q. Chen, W. Z. Shi, G. Li and Y. Yang, *Adv. Mater.*, 2016, **28**, 2253.

50. Y. Liu, Y. Zhang, Z. Yang, J. Feng, Z. Xu, Q. Li, M. Hu, H. Ye, X. Zhang, M. Liu, K. Zhao and S. Liu, *Materials Today*, 2019, **22**, 67.

51. F. M. Li, W. D. Zhu, C. X. Bao, T. Yu, Y. Q. Wang, X. X. Zhou and Z. G. Zou, *Chem. Commun.*, 2016, **52**, 5394.

52. T. Jeon, H. M. Jin, S. H. Lee, J. M. Lee, H. I. Park, M. K. Kim, K. J. Lee, B. Shin and S. O. Kim, *ACS Nano*, 2016, **10**, 7907.

53. J. Troughton, M. J. Carnie, M. L. Davies, C. Charbonneau, E. H. Jewell, D. A. Worsley and T. M. Watson, *J. Mater. Chem. A*, 2016, **4**, 3471.

54. S. Sanchez, X. Hua, N. Phung, U. Steiner and A. Abate, *Adv. Energy Mater.*, 2018, **8**, 1702915.

55. Y. Z. Wu, F. X. Xie, H. Chen, X. D. Yang, H. M. Su, M. L. Cai, Z. M. Zhou, T. Noda and L. Y. Han, *Adv. Mater.*, 2017, **29**, 1701073.

56. P. You, Z. K. Liu, Q. D. Tai, S. H. Liu and F. Yan, *Adv. Mater.*, 2015, **27**, 3632.

57. Y. H. Shao, Z. G. Xiao, C. Bi, Y. B. Yuan and J. S. Huang, *Nat. Commun.*, 2014, **5**, 5784.

58. D. Q. Bi, C. Y. Yi, J. S. Luo, J. D. Decoppet, F. Zhang, S. M. Zakeeruddin, X. Li, A. Hagfeldt and M. Gratzel, *Nat. Energy*, 2016, **1**, 16142.

59. P. Docampo, F. C. Hanusch, N. Giesbrecht, P. Angloher, A. Ivanova and T. Bein, *APL Mater.*, 2014, **2**, 081508.

View Article Online

DOI: 10.1039/C9EE02324K

60. Z. N. Song, S. C. Watthage, A. B. Phillips, B. L. Tompkins, R. J. Ellingson and M. J. Heben, *Chem. Mater.*, 2015, **27**, 4612.

61. D. Bi, W. Tress, M. I. Dar, P. Gao, J. Luo, C. Renevier, K. Schenk, A. Abate, F. Giordano, J.-P. C. Baena, J.-D. Decoppet, S. M. Zakeeruddin, M. K. Nazeeruddin, M. Grätzel and A. Hagfelddt, *Sci. Adv.*, 2016, **2**, 1501170.

62. D. W. deQuilettes, S. M. Vorpahl, S. D. Stranks, H. Nagaoka, G. E. Eperon, M. E. Ziffer, H. J. Snaith and D. S. Ginger, *Science*, 2015, **348**, 683.

63. J. Bisquert, L. Bertoluzzi, I. Mora-Sero and G. Garcia-Belmonte, *J. Phys. Chem. C*, 2014, **118**, 18983.

64. Q. D. Tai, P. You, H. Q. Sang, Z. K. Liu, C. L. Hu, H. L. W. Chan and F. Yan, *Nat. Commun.*, 2016, **7**, 11105.

65. G. Q. Tang, P. You, Q. D. Tai, R. S. Wu and F. Yan, *Sol Rrl*, 2018, **2**, 1800066.

66. E. Aydin, M. De Bastiani and S. De Wolf, *Adv. Mater.*, 2019, **31**, e1900428.

67. X. Meng, J. Lin, X. Liu, X. He, Y. Wang, T. Noda, T. Wu, X. Yang and L. Han, *Adv. Mater.*, 2019, DOI: 10.1002/adma.201903721, 1903721.

68. S. Zhang, S. M. Hosseini, R. Gunder, A. Petsiuk, P. Caprioglio, C. M. Wolff, S. Shoaee, P. Meredith, S. Schorr, T. Unold, P. L. Burn, D. Neher and M. Stolterfoht, *Adv. Mater.*, 2019, **31**, 1901090.

69. M. Ledinsky, T. Schonfeldova, J. Holovsky, E. Aydin, Z. Hajkova, L. Landova, N. Neykova, A. Fejfar and S. De Wolf, *J. Phys. Chem. Lett.*, 2019, **10**, 1368.

70. S. De Wolf, J. Holovsky, S. J. Moon, P. Loper, B. Niesen, M. Ledinsky, F. J. Haug, J. H. Yum and C. Ballif, *J. Phys. Chem. Lett.*, 2014, **5**, 1035.

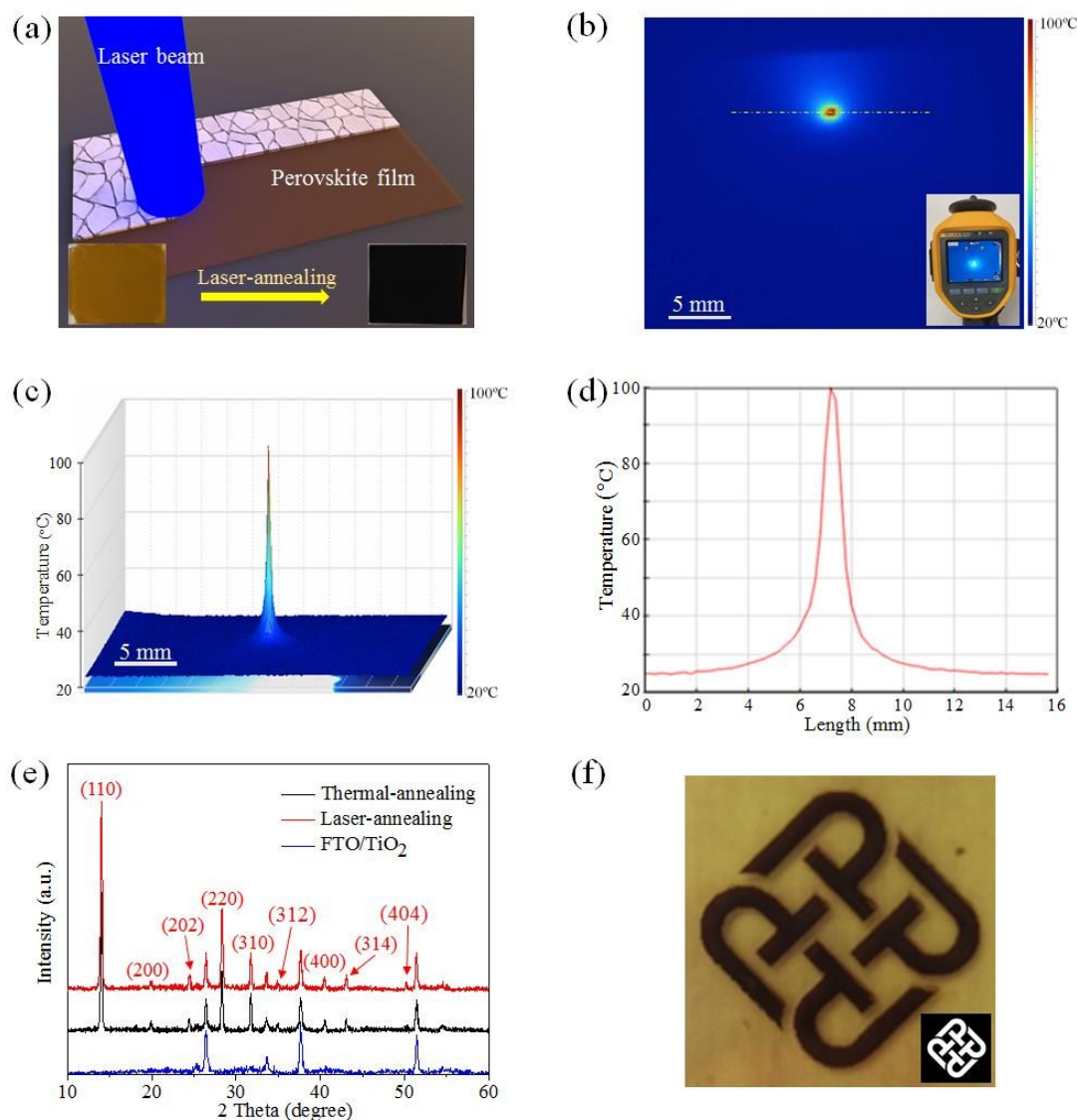## COMMUNICATION

Figures:

Figure 1. (a) Schematic illustration of the laser annealing process. Inset shows photos of the as-deposited (left) and laser-annealed (right) perovskite films. (b,c) 2D and 3D infrared thermal images of the MAPbI$_3$ perovskite film surface during the laser annealing process (450-nm laser, 150 mW, 25 mm/min). Inset shows the infrared thermal imager used here. (d) Temperature distribution on the MAPbI$_3$ perovskite film surface along the dash line in Figure 1b. (e) XRD spectra of FTO/TiO$_2$ and FTO/TiO$_2$/MAPbI$_3$ films. (f) MAPbI$_3$ perovskite film patterned with focused laser beam. Inset shows the black-white picture used as template for laser patterning process.
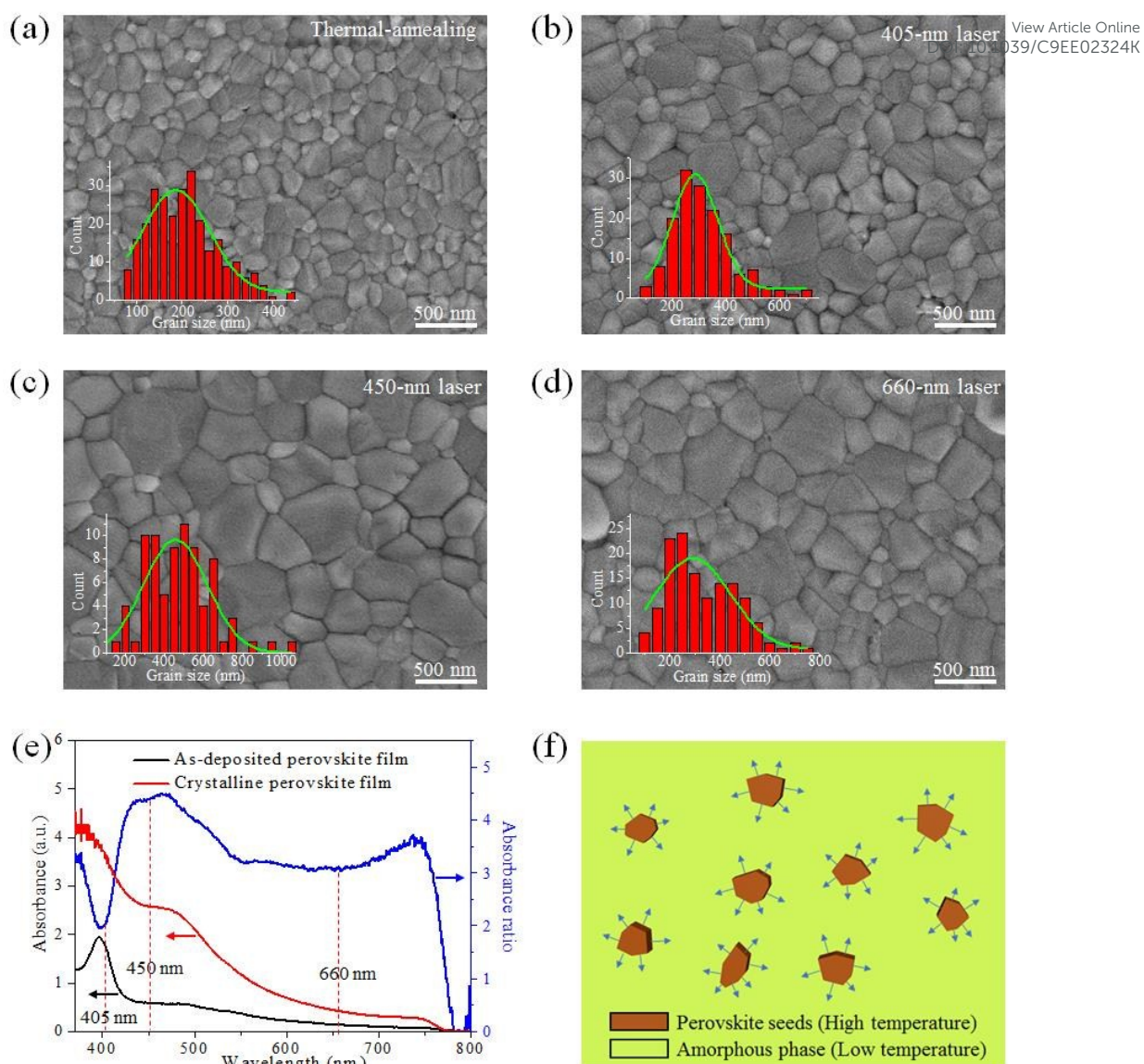
Figure 2. (a-d) Plan-view SEM images of MAPbI$_3$ perovskite films fabricated by thermal-annealing and laser-annealing processes. 405-nm, 450-nm and 660-nm lasers were used here. Insets show the statistical diagrams of the grain size distribution based on the SEM images. (e) UV-vis absorbance spectra of the as-deposited and laser-annealed MAPbI$_3$ perovskite films, along with the absorbance ratio between the two films. (f) Schematic diagram of the perovskite crystallization process under the illumination of laser beams. Arrows show growth directions of perovskite grains.
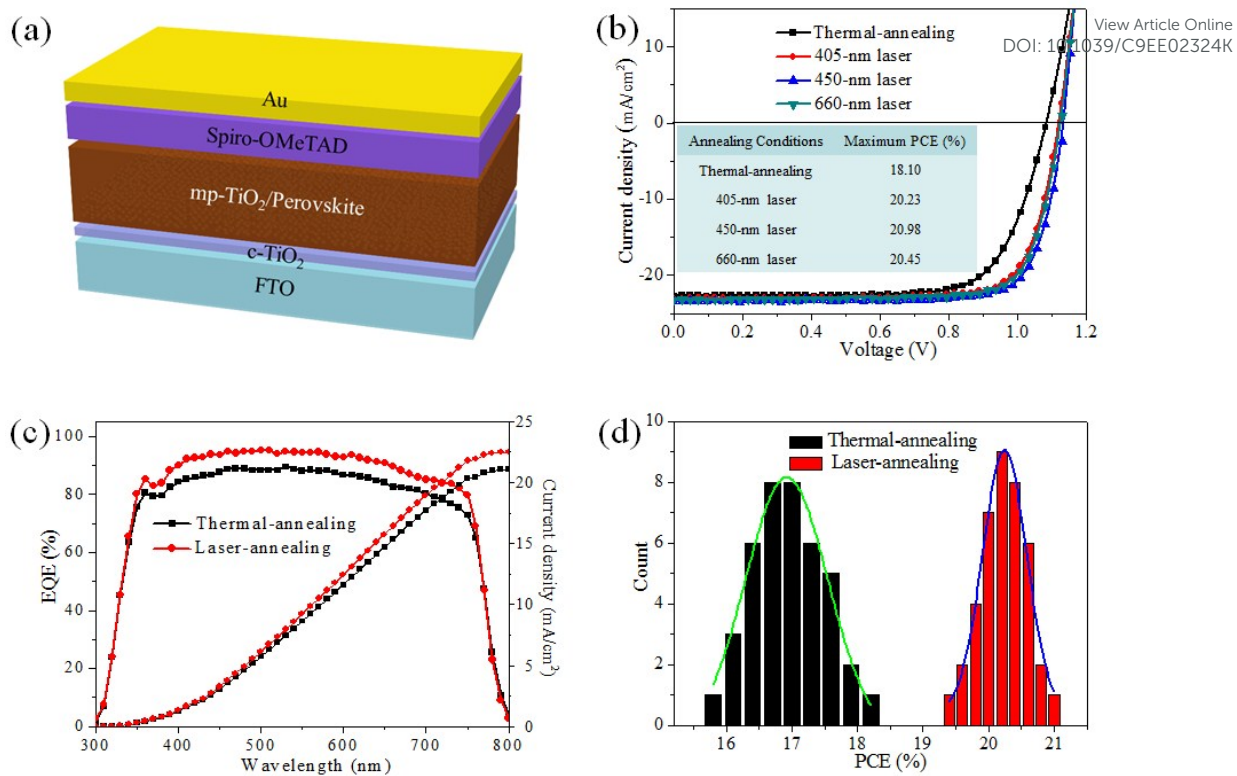
Figure 3. (a) Schematic diagram of the solar cell structure. (b) *J-V* curves and (c) EQE spectra of the best MAPbI$_3$ PSCs fabricated by thermal-annealing and laser-annealing processes. (d) Histogram of PCEs derived from the reverse scans of 40 devices fabricated at the optimum conditions.
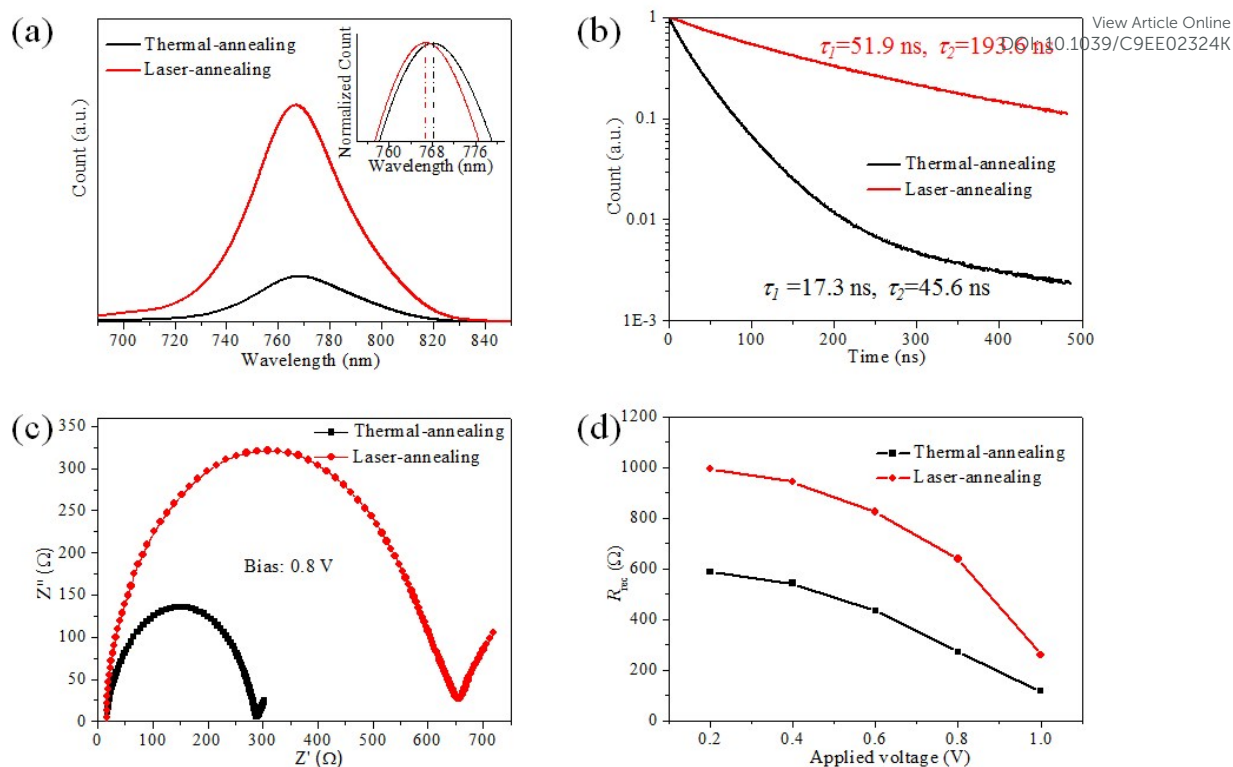
Energy & Environmental Science Accepted Manuscript

Figure 4. (a) Steady-state photoluminescence (PL) spectra and (b) time-resolved PL spectra of MAPbI$_3$ perovskite films prepared by thermal-annealing and laser-annealing approaches. (c) Electrochemical impedance spectra of MAPbI$_3$ PSCs measured at a bias voltage of 0.80 V under light illumination of 100 mW/cm^2 (white light). (d) The recombination resistance of the MAPbI$_3$ PSCs derived from impedance spectra biased at different voltages under light illumination of 100 mW/cm^2.
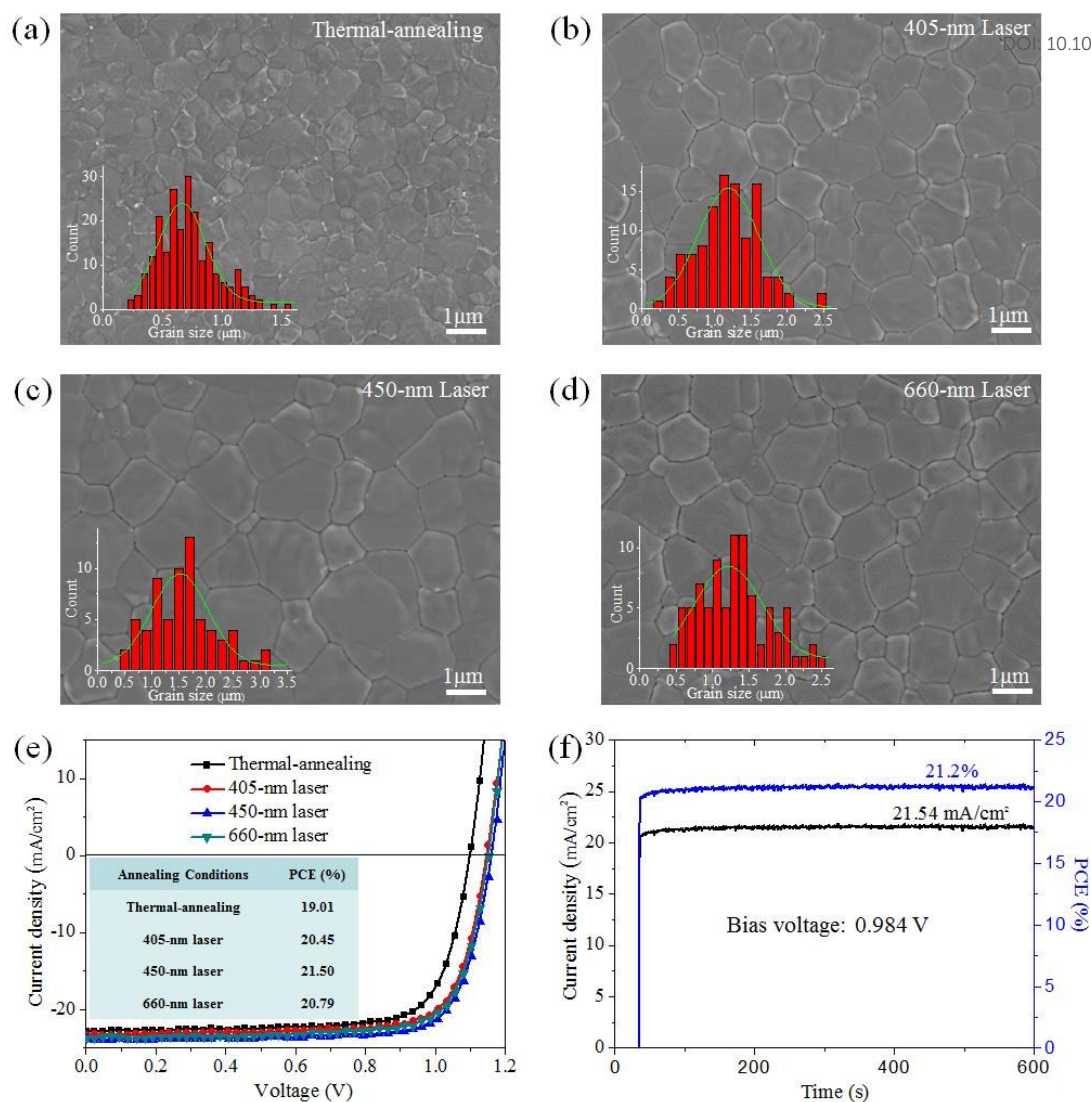
Figure 5. (a-d) SEM images of the mixed perovskite films fabricated by thermal-annealing and laser-annealing processes. 405-nm, 450-nm and 660-nm lasers were used here. Insets show the statistical diagrams of the grain size distribution based on the SEM images. (e) *J-V* curves of the best devices fabricated by thermal-annealing and laser-annealing processes. (f). Steady-state photocurrent and efficiency of the champion device measured at the maximum power point.

Tables:

Table 1. Photovoltaic parameters of MAPbI$_3$ PSCs fabricated by thermal-annealing and laser-annealing (with different laser wavelengths) processes. (Average of no less than 20 cells for each condition.)

	Laser wavelengths	V_{OC} (V)	J_{SC} (mA/cm²)	FF (%)	PCE (%)	Champion PCE (%)
Thermal-annealing	--	1.069±0.011	22.36±0.47	70.64±2.02	16.89±0.72	18.10
Laser-annealing	405 nm	1.112±0.009	23.18±0.21	76.44±1.24	19.71±0.38	20.23
	450 nm	1.124±0.009	23.29±0.20	77.27±1.16	20.23±0.35	20.98
	660 nm	1.119±0.008	23.22±0.21	76.68±1.17	19.92±0.38	20.45

Table 2. Photovoltaic parameters of the mixed PSCs fabricated by thermal-annealing and laser-annealing processes. (Average of no less than 20 cells for each condition.)

	Laser wavelengths	V_{OC} (V)	J_{SC} (mA/cm²)	FF (%)	PCE (%)	Champion PCE (%)
Thermal-annealing	--	1.09±0.01	22.83±0.46	73.10±1.18	18.22±0.46	19.01
Laser-annealing	405 nm	1.13±0.01	23.56±0.34	76.60±0.84	20.19±0.32	20.45
	450 nm	1.14±0.01	23.56±0.21	77.44±0.69	20.82±0.31	21.50
	660 nm	1.14±0.01	23.40±0.26	76.68±0.65	20.44±0.30	20.79

TOC Figure:
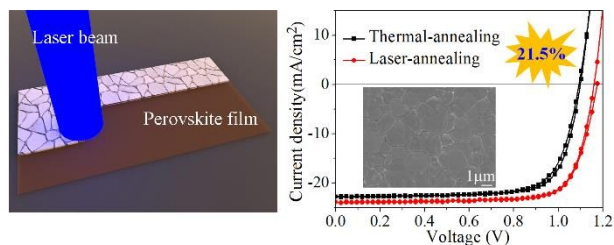
Ultrafast laser-annealing technique for the fabrication of large-grain perovskite films and efficient perovskite solar cells at room temperature.

Broader context

Perovskite solar cells have attracted much attention recently due to their high efficiency, low cost and convenient fabrication processes. Perovskite films are normally prepared by thermal annealing for a long period of time (about 1 hour), which is time and energy consuming and incompatible with low-temperature fabrication required by certain devices such as flexible solar cells on plastic substrates. In this work, we demonstrate an ultrafast perovskite annealing strategy by scanning a laser spot on the film surface with a speed of tens of millimeter per minute. The fast scanning of the laser spot on the perovskite surface induces high temperature gradient in the perovskite film, which can accelerate the growth of perovskite grains in a short period of time (only several second) while the substrate is maintained at the room temperature. The resultant devices show high efficiency (over 21%) and good stability due to the high quality of the perovskite films under laser annealing. More importantly, this fast annealing approach can be used in the fabrication of large-area perovskite solar cells by utilizing linear laser. Therefore, the ultrafast laser scanning method is a promising technique for the mass production of perovskite solar cells with low cost.